Journal of Energy Storage 106 (2025) 114901

Contents lists available at ScienceDirect

Journal of Energy Storage

journal homepage: www.elsevier.com/locate/est

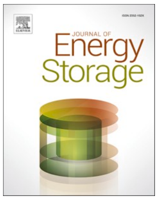

Research papers

Monitoring and assessment of the thermomechanical performance of a concrete layer section of a thermocline tank

T. Lucio-Martin [a], T. Grandal [b], M. Roig-Flores [a,d], R.S. Villardón [c], Luis Guerreiro [e], M.C. Alonso [a,*]

[a] *Consejo Superior de Investigaciones Científicas, Eduardo Torroja Institute for Construction Sciences (CSIC-IETcc), Madrid, Spain*
[b] *Aimen Technology Center, Pontevedra, Spain*
[c] *ACCIONA Ingeniería, Madrid, Spain*
[d] *Universitat Jaume I, Department of Mechanic Engineering and Construction, Castellón de la Plana, Spain*
[e] *ICT – Institute of Earth Sciences, University of Évora, Évora, Portugal*

ARTICLE INFO

Keywords:
Thermocline tank
Concrete
Monitoring
fiber optic sensors
Electrical resistance
Thermal energy storage

ABSTRACT

In previous research, a hybrid steel-concrete tank section for Thermal Energy Storage (TES) was built and operated as a thermocline tank, indicating that the concrete section demonstrated its suitability and good thermal response under repetitive thermal fatigue cycles. In this investigation, the effect of the high temperature in the Calcium Aluminate Cement concrete (CAC) layer has been analysed in detail for the preconditioning, commissioning, during thermal fatigue operation and after the thermal cycling. For that purpose, 2 different types of instrumentation were used for the monitoring of thermal and mechanical response: conventional thermocouples and innovative Fiber Bragg Grating (FBG) sensors to measure both temperature and strain at high temperatures continuously. Besides, a protocol for monitoring the commissioning and operation of the concrete tank the electrical resistance (ER) of the CAC layer at high temperatures was measured to control the drying process. Moreover, some visual and physicochemical tests were carried out after the thermal performance to evaluate the effect of the heat across the concrete layer. The findings showed that the used of CAC concrete withstands the heating and cooling cycles between 200 and 500 °C and the appropriateness of using FBG sensors has been fully demonstrated. The measure of the ER is a useful tool for following the drying process and temperature cycling operation.

Nomenclature

Acronyms

AG	Air Gap
ATD	Thermogravimetric analysis
CAC	Calcium Aluminate Cement
CSP	Concentrating Solar Power
CTES	Concrete as a Thermal Energy Storage
DRX	X-Ray diffraction
FBG	Fiber Bragg Gratings
FOS	Fiber Optic Sensor
HHM	Higher Heating Mat
HTF	Heat Transfer Fluid
IL	Interface Layer
LHM	Lower Heating Mat
PPF	Polypropylene Fibres
SDG	Sustainable Development Goals
TES	Thermal Energy Storage
UPV	Ultrasonic Pulse Velocity
w/c	Water/Cement Ratio

1. Introduction

The interest in replacing the energy consumption model has been raising lately. An Energy and ecological transition is being promoted by world leaders around the world aiming to achieve affordable, reliable, sustainable forms of renewable energy as stated in the 7th Sustainable

---

[*] Corresponding author at: Consejo Superior de Investigaciones Científicas, Eduardo Torroja Institute for Construction Sciences (CSIC-IETcc), Calle de Serrano Galvache, 4, 28033 Madrid, (Spain).

E-mail address: mcalonso@ietcc.csic.es (M.C. Alonso).

https://doi.org/10.1016/j.est.2024.114901
Received 5 July 2024; Received in revised form 7 October 2024; Accepted 30 November 2024

Development Goals (SDG) fixed by the United Nations by 2030 [1]. Renewable energies and energy efficiency play an important role as well as energy storage systems in order to provide energy with a high level of dispatchability that is, able to be provided when it is demanded [2].

Previous research has demonstrated the usefulness of using concrete as a thermal energy storage material (CTES) at moderate temperatures [3–5] and high temperatures up to 550 °C [6–8]. However, the performance has been proved in small concrete specimens and its viability at a bigger scale has not been sufficiently assessed at those high temperatures, to the knowledge of the authors. The use of concrete for Thermal Energy Storage (TES) in modules has been proven in prototypes up to 400 °C [9,10]. However, the molten salts used as a heat transfer fluid (HTF) in Concentrating Solar Power (CSP) Plants can be operated at temperatures between the melting point and the maximum temperature without degradation of the salt, usually between 290 and 550 °C for the so called "Solar Salt" [2,11,12]. In addition, a new study has demonstrated the use of the Solar Salt at temperatures up to 600 °C [13]. For that reason, the TES infrastructures need to be operated at higher temperatures to store more energy.

Concrete is a material that can be used in TES infrastructures as a TES material, as a structural element or to have a refractory or insulating applications. The desired properties for this material vary with its function in the infrastructure and its location. Recent studies used concrete as a silo container for storing particles at high temperatures, but it functions as a structural element and the maximum temperature reached at the concrete level is below 90 °C [14]. Other studies have demonstrated the use of concrete as a medium of TES in thermocline tanks at temperatures up to 600 °C [15]. However, the use of concrete as a structural element of thermocline tanks has not been proved up to date and it is the main goal of the research performed.

The most common material used in the tanks of the systems with two tanks of molten salts used in Concentrated Solar Power (CSP) is steel. The aim of this investigation is to verify the possibility of replacing this steel by concrete, whose main advantages are a lower cost and it can be produced onsite easy to adapt to the required size and available worldwide [7]. The desired requirements of concrete for this specific application are the ability to withstand high temperatures up to 600 °C and cyclic conditions. Furthermore, the use of a single thermocline tank instead of two-tanks has been proved to reduce the cost of the TES facility. In the case of a thermocline tank, the concrete structure needs to resist thermal gradients along the longitudinal section of the concrete wall due to the continuous charge and discharge of energy, which influences the tank stability as it was reported in previous studies [16,17].

This investigation analyses the feasibility of using concrete as a structural material in a thermocline tank and discusses the effect of the heat at different depths to the heat source. The research focuses on the absence of extensive experience in commissioning and testing such concrete infrastructures at larger scale. A prior study analysed the experimental assessment of an upscaled section of a thermocline tank simulating the operating conditions with temperatures between 200 and 500 °C [18]. The study detailed the construction and operation of the upscaled infrastructure made of concrete, rockwool and a steel liner. The commissioning and the thermal performance during the thermal cycles across the tank were analysed in the whole system. The study demonstrated that the joint system worked, and the concrete layer withstood the high temperatures and heating and cooling cycles. The present investigation focuses on the specific behaviour of the concrete layer and its response when it is exposed to thermal cycles and gradients.

The cement selected in this study was Calcium Aluminate Cement (CAC) to produce a high thermal resistance concrete, which in previous research has proved to be thermally stable to heating and cooling cycles up to 550 °C [18–20]. When concrete is exposed to high temperatures, some physicochemical changes takes place due to the dehydration of the cement paste, the loss of the free water and variations of volume owing to the expansion and shrinkage of its components [21,22]. The thermal response of the concrete varies with the type of cement. In particular, the CAC of this investigation, at temperatures up to 100 °C starts the drying process and concrete loses the free water of its pores. The CAC paste is progressively losing the chemically bound water (dehydration) up to 300 °C with the decomposition of hydrated phases (CAH_{10} and AH_3). At higher temperatures, the expansion of the aggregates and shrinkage of the dehydrated cement paste takes place [21,22]. In addition, the spalling phenomenon might occur due to the internal thermal stresses undergone for the expansion loads at high temperatures and pressures due to accumulation of water vapour in pores. In previous research done at smaller scale, CAC concretes have proved to be thermally stable to heating and cooling cycles up to 550 °C [7,18–20], and it can have higher compressive strength and elastic modulus than OPC concretes at temperatures between 20 °C–800 °C [23].

On the other hand, the spalling phenomenon might occur due to the internal pressures or thermal gradients produced at high temperatures. An aspect addressed in [18] was a forced drying process of concrete to minimize the risk of spalling by eliminating the free water in the pores. The monitoring of the drying process can be performed through the measure of electrical response of concrete with the temperature, which has the advantage of being a non-destructive test method. Previous experimental tests carried out at lab-scale with small specimens have demonstrated its potential of monitoring the drying process of CAC by measuring its electrical resistance [24,25]. Concrete is a composite material composed mainly by aggregates (gravel and sand), cement paste, pores (with water and or air) and fibres, among others. There are interconnected channels between the cement paste and the water and air pores. When concrete is saturated, the ionic transport occurs mainly through the liquid in the pores and the vascular network created [26]. When the temperature increases, the specimen experienced changes in its volume, which modifies the distance within the material. Moreover, the temperature will change the transition energy of the electrons, resulting in a variation in the water content and the moisture of concrete in the pores [27]. Once the concrete has lost all the free water, the electrical transfer through ions is mainly affected by the characteristics of the other components such as the solid phases. Therefore, the measure of the electrical resistance can be useful to determine how the drying and the temperature cycling are affecting the interconnection among pores and to detect cracks within the material [24].

To have a proper operation of the facility it is important to have an appropriate monitoring system of the response of the structure when is exposed to heat. For that purpose, following the evolution of critical parameters that affect the stability of the concrete tank as temperature and strain is relevant to know how the structure is being responded in real-time and to take decisions. The monitoring of temperature is usually performed based on point temperature sensors as thermocouples or PT100, while despite strain monitoring of heat and cycling is very relevant, there is a lack of experience in this parameter [28,29]. In this investigation, innovative Fiber Bragg Grating (FBG) sensors, able to measure temperature and strain, embedded in the concrete in real-time were used. For this purpose, ad-hoc Fiber Bragg Grating (FBG) sensors were designed and developed to be embedded directly in the CAC concrete matrix and to monitor strain and temperature at real-time. In addition to temperature FBG sensors, conventional thermocouples were also integrated, in order to validate the use of both sensors in the performance of up-scaled thermocline tanks at high temperatures. Fiber optic sensors have a strong history in Structural Health Monitoring (SHM) for civil structures, particularly in concrete applications such as bridges, pillars, dikes, and tunnels [30,31]. Their resistance to electromagnetic interference and robustness in harsh environments make them ideal for such purposes. However, their small size and fragility pose challenges for installation in demanding conditions. Protective encapsulates have been developed to address this issue. The encapsulation process is crucial for accurate measurements, as poor encapsulation can lead to incorrect readings. Researchers have focused on developing suitable encapsulation materials to enhance sensor durability and expand monitoring capabilities beyond temperature and strain for concrete applications operating at room temperatures (environmental temperatures) [32–34]. In applications where the concrete reaches temperatures up to 500 °C, improved coatings or packaging are necessary to ensure sensor performance. In this work, fiber optic sensors based on FBGs were embedded directly in contact with CAC concrete using special (ad-hoc developed) metallic packaging and coatings to resist the embedding and operation process.

This article aims to improve the knowledge on the use of concrete for a thermocline tank TES infrastructure. It provides a practical application at a bigger scale in order to put into practice the suitability of the concrete mix (and monitoring tools) for the thermal performance during the preconditioning, commissioning and testing under a typical CSP Plant regime. After the thermal performance test, the concrete layer was also studied through a visual inspection and physicochemical tests. Additionally, the present investigation aims to improve the knowledge in the monitoring of concrete infrastructures at high temperatures, especially strain, by using FBG sensors.

To recap, the novelties of this work are: 1) to demonstrate the usefulness of using concrete for a thermocline tank in an upscale prototype, 2) to provide some proper preconditioning and commissioning testing at upscaled and 3) to monitor the thermos-mechanical performance with thermocouples, FGB sensors and electrical resistance monitored at high temperatures on real-time.

2. Experimental setup and methodology

2.1. Materials

A section of a thermocline tank made of concrete has been fabricated to monitor the performance at high temperatures and during thermal fatigue cycles between 200 and 500 °C. The prototype section evaluated comprises different layers: 1) 2 heating mats as a heat source, simulating the heat from the molten salts, 2) a thin steel liner, simulating the container of salts, 3) an interface of air to allow thermal expansions during the operation, 4) a concrete element as part of the tank infrastructure, whose dimensions are 1000x500x300 mm^3, and 5) insulating materials such as rockwool at top and lateral faces and expanded clay at foundations to minimize the heat losses to the surroundings. The thermal response of the complete system was reported previously [18] and this investigation focuses on the response of the concrete element as part of the tank wall infrastructure.

Regarding the concrete element, CAC cement was used due to its refractory properties and good response at high temperatures [21]. The aggregates used in the composition are: fine CAT, from CAC clinker crushing and coarse basalt aggregates, and a waste Slag from *São Domingos mine* [35,36]. The composition also contained polypropylene fibres (PPF) to reduce the risk of spalling [37]. The composition of the concrete mix is detailed in Table 1.

2.2. Methodology

2.2.1. Process manufacturing

The dimensions of the concrete specimen are 1000x500x300 mm^3. One batch of concrete of 230 l was prepared in a tilting drum mixer. The tests done to characterize the concrete mix are consistent by means of the slump test (EN 12350–2:2009), initial and 40 min after mixing, and compression strength (EN 12390–3:2009) after curing for 7 days measured in 3 specimens from the same batch. The initial slump test obtained is 150 mm and after 40 min of mixing the slump test was 170 mm (Fig. 1.a). Thus, the concrete produced showed high flowability and a consistency class of between S3 (100–150 mm) and S4 (160 and 210 mm). Despite this high flowability, concrete was vibrated inside the tank section formwork with a vibration needle, due to the high density of sensors and thermocouples some could change its initial position, as shown later, in order to ensure concrete compactness. Compression strength was tested in cylindrical samples of Φ150 x H300 mm, resulting in 48 MPa at the age of 7 days.

Table 1
Composition of the CAC concrete.

Concrete composition	kg/m^3
Cement CAC	600
Water	258
Basalt gravel 4–12 mm	682
Slag gravel 3–7 mm	139
CAT sand 0–3 mm	714
Slag sand 0.25–2 mm	128
Polypropylene fibres (PPF)	2
Plasticizer	0.9
Water/cement (w/c)	*0.43*

After concrete pouring and compacting, the element was covered in rock-wool and wood panels to avoid water evaporation during the setting and hardening processes of the element (Fig. 1.b). Six days after casting, the element was demoulded, and the final appearance of the element showed no visible defects (Fig. 1.c). The brown dots observed on the surface are typical from this type of material and do not indicate the presence or defects nor holes.

2.2.2. Instrumentation and final arrangement of the concrete prototype

The aim of the instrumentation is to evaluate how heat flow varies through the concrete layer, obtaining the temperature profile and deformations produced by the heat exposure. For that purpose, the CAC concrete layer had embedded temperature and strain FBGs and conventional thermocouples, which are recording temperature and strain parameters during the monitoring stage. In addition, electrical resistance measurements were performed using the metallic encapsulation of the temperature FBGs to complement the information provided by the FBG sensors and thermocouples. The detail of sensor connectors is shown in Fig. 1.d.

An FBG is a periodic structure within an optical fiber where the refractive index of the core periodically changes along its length. This periodic variation forms a diffraction grating that reflects a specific wavelength of light while allowing other wavelengths to pass through. The reflected wavelength is called the Bragg wavelength, and it is determined by the period of the grating. When the physical parameter (e.g., strain or temperature) changes, it induces a strain or temperature-dependent shift in the Bragg wavelength of the grating. By measuring this wavelength shift, the corresponding physical parameter can be accurately determined. FBG sensors were selected because they offer advantages such as high sensitivity, high temperature resistance, and the ability to multiplex multiple sensors along a single optical fiber. These characteristics make FBG sensors valuable in various applications, including structural health monitoring, aerospace, civil engineering, and industrial process control. To make the FBGs robust to be embedded in this high thermal resistance concrete, they were coated with a metal, Ni, for the case of the strain FBGs and encapsulated in a capillary tube of stainless steel SS316L type with 3.2 mm of external diameter for the temperature FBGs (Fig. 2). In the work presented here, multiplexed and single FBGs were embedded at different locations and depths of the CAC concrete layer to measure both temperature and strain variations. A total of seven different fiber sensor arrays were embedded, each one of them formed by 3 FBGs. Accordingly, a total of 21 polyimide coated FBGs were employed to monitor the temperature variations inside the concrete sample. The temperature sensors were embedded using 316 stainless steel capillaries, to avoid strain sensitivity. Furthermore, five more FBGs, coated with Ni up to 600 μm of total diameter, were embedded (directly) to monitor the strain of the of the CAC concrete. Moreover, the stainless steel capillaries were used to measure the response of the electrical resistance of concrete during the thermal exposure.

Additionally, some thermocouples were located close to temperature FBGs to validate their measurements and also, in the boundaries of the

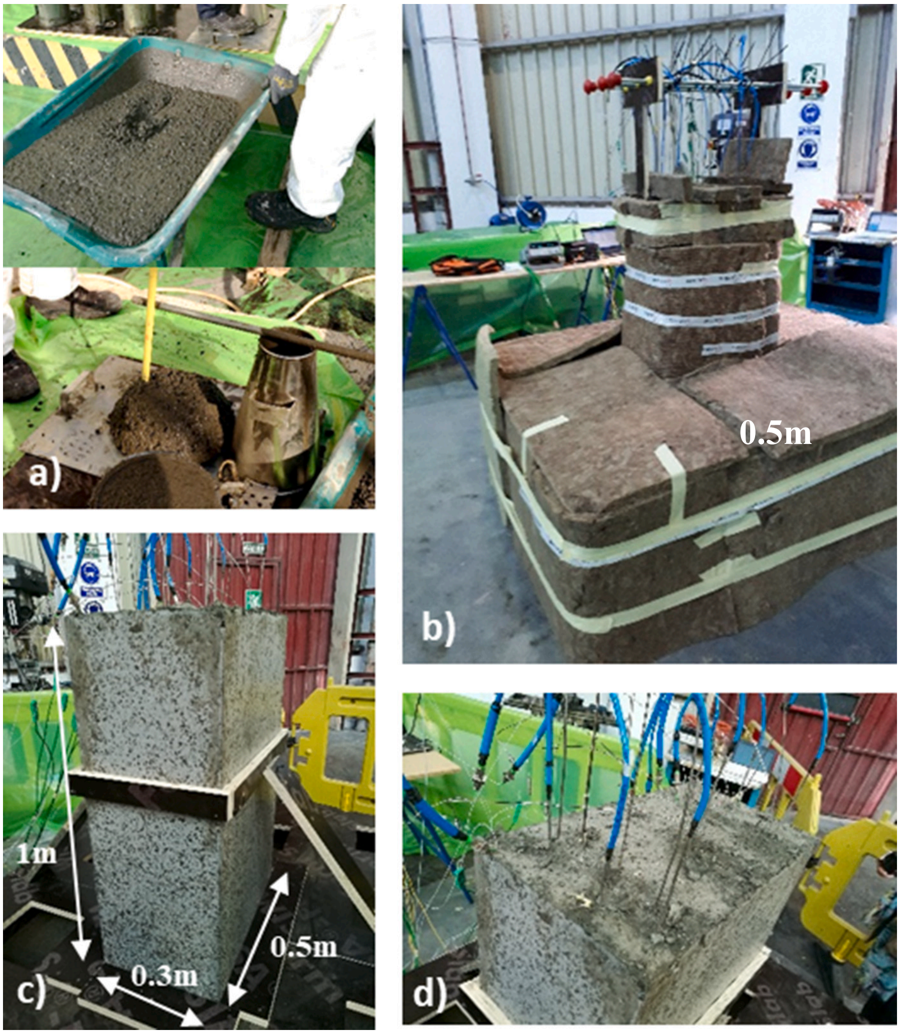

Fig. 1. Setting and hardening processes of the concrete layer: a) CAC concrete mix: mix appearance and second slump test, b) CAC concrete layer covered in wood and rockwool panels, c) CAC concrete layer after demolding with dimensions, d) detail of the sensors connectors (FBGs and thermocouples) after demolding.

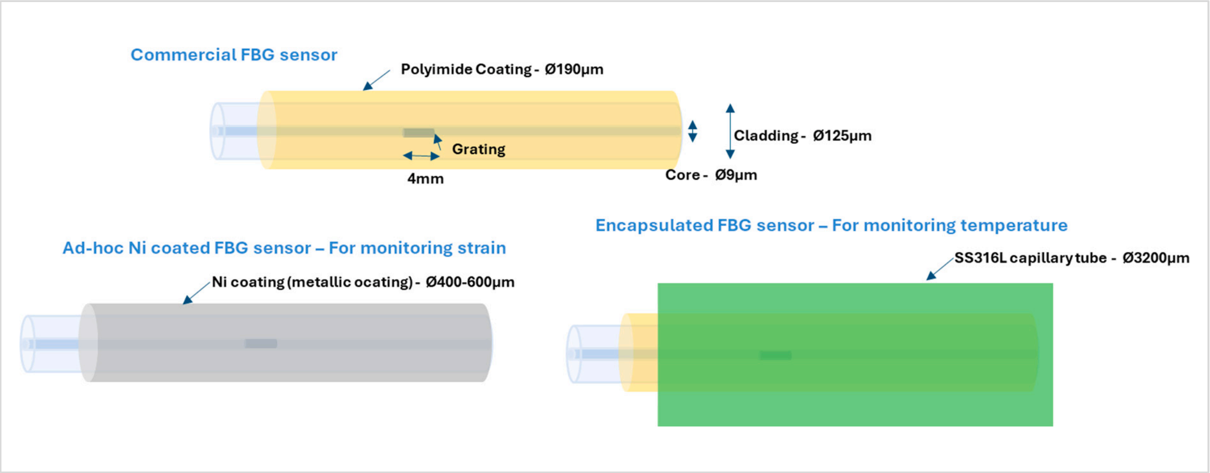

Fig. 2. Scheme of FBG sensors developed for this work.

element, named interface layers (IL) to record and quantify the temperature profile across the full section. IL1 in Fig. 3.a represents the interface between the air gap and the part of the concrete closer to the heat source, whereas IL2 indicates the interface between the rear part of the concrete layer and the insulating material. On the other hand, the whole system was isolated with Rockwool so as to reduce heat losses to the environment.

The coordinates and depths of embedded FBG sensors and

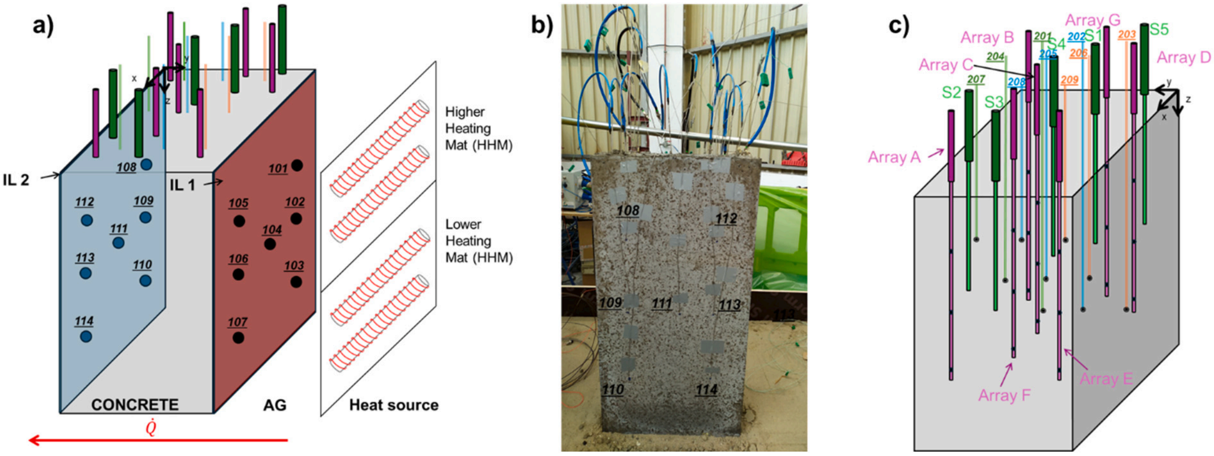

Fig. 3. a) Instrumentation with external thermocouples between layers, b) External surface of one concrete layer with the thermocouples glued with high temperature adhesive to this surface, c) Schematic position of thermocouples and FGB sensors embedded in the concrete section.

thermocouples are included in Table 2, while the coordinates of external (surface) thermocouples are included in Table 3. Fig. 3.b shows the setup of the external thermocouples in the boundary IL2 between layers and Fig. 3.c shows the schematic position of the thermocouples and FGB sensors embedded in the concrete element.

The electrical heating mats used to simulate the heat source are high temperature flexible heating mats, standardized SXH models, FGH-18 × 18–2-A, 4.212 Watios, from Electricfor, S.A. The maximum temperature that mats withstand is 500 °C and it has a control system able to make the heating and cooling processes with a controlled time and heating rates. The accuracy of the programmed temperature of the heat source was ±1 °C, and the heating rate was 1 °C/min. The measurements of temperature with the calibrated K-type thermocouples have an accuracy of ±0.1 °C. All temperature data collected by conventional thermocouples were recorded with a data acquisition system (Model: Agilent 34970 A). Regarding the FBG sensors, two sm125 MicornOptics interrogator was used. Composed by 4 channels and an acquisition frequency up to 1000 Hz. A schema of the instrumentation is included in Fig. 3.a.

Finally, Fig. 3.b shows the appearance of one of the surfaces of the concrete layer, with the disposition of FBG sensors and thermocouples.

Table 3
Coordinates of external thermocouples.

Temperature sensors: Conventional thermocouples							
Surface IL1				Surface IL2			
Name	Location (mm)			Name	Location (mm)		
	X	Y	Z		X	Y	Z
101	120	0	250	108	100	300	250
102	120	0	500	109	100	300	500
103	120	0	750	110	100	300	750
104	230	0	500	111	270	300	500
105	400	0	250	112	380	300	250
106	400	0	500	113	380	300	500
107	400	0	750	114	380	300	750

2.2.3. *Thermal regime*

The commonly two-tanks in a CSP plant store molten salts between 290 and 600 °C [2,11,13]. For that reason, the infrastructure needs to withstand the heating and cooling cycles at high temperatures. For that

Table 2
Coordinates of embedded thermocouples and FGB sensors.

Temperature sensors									
Name	Kind of sensor	Location (mm)			Name	Kind of sensor	Location (mm)		
		X	Y	Z			X	Y	Z
Array A	Fiber optic sensor	395	220	750	201	Thermocouples	100	245	750
				500	202	Thermocouples	100	160	750
				250	203	Thermocouples	100	60	750
Array B	Fiber optic sensor	75	220	750	204	Thermocouples	270	245	500
				500	205	Thermocouples	270	160	500
				250	206	Thermocouples	270	60	500
Array C	Fiber optic sensor	265	140	750	207	Thermocouples	365	245	250
				500	208	Thermocouples	365	160	250
				250	209	Thermocouples	365	60	250
Array D	Fiber optic sensor	105	60	750					
				500	Strain fiber optic sensors				
				250	Name	Kind of sensor	Location (mm)		
							X	Y	Z
Array E	Fiber optic sensor	395	60	750	S1	Fiber optic sensor	105	140	500
				500	S2	Fiber optic sensor	365	220	500
				250	S3	Fiber optic sensor	395	140	500
Array F	Fiber optic sensor	447	140	750	S4	Fiber optic sensor	235	140	500
				500	S5	Fiber optic sensor	75	60	500
				250					
Array G	Fiber optic sensor	105	140	750					
				500					
				250					

purpose, this work deals with a simulation of a real scenario of a thermocline tank where the operating regime ranges between 200 and 500 °C. The limits of temperature were chosen to operate with a ΔT of 300 °C due to the heat source (mats) was not able to be reach 600 °C.

There are no experiences of tanks for thermal energy storage made of concrete, to the knowledge of the authors. However, some studies conclude its appropriateness for this application based on results at lab-scale [6,7] and in modular prototypes but at lower temperatures, up to 400 °C [10,38]. Focusing on this prototype, the CAC concrete layer is the most critical point owing to the physical and chemical transformations that take place at high temperatures [21,22]. For that reason, the heat flux effect was assessed in two stages: 1) drying + dehydration and 2) thermal fatigue during the operation of the thermocline prototype.

2.2.3.1. Drying and dehydration curve. A minimum maturity of concrete of at least 28 days is recommended to start with the thermal performance. The concrete had a maturity of 188 days before starting the test. The thermal cycle of the drying and dehydration stage is shown in Fig. 4. Firstly, the temperature increases up to 100 °C to produce the loss of free water of concrete and the drying process. After that, so as to produce the dehydration of the concrete, two plateaus of constant temperature at 200 and 300 °C are established in order to make the temperature homogeneous and to avoid high thermal gradients within the concrete layer, which might produce the spalling phenomenon. The time at the plateaus is defined during the test and will be determined by the response of the sensors embedded in the concrete layer.

2.2.3.2. Thermal fatigue curve. The thermal fatigue stage covers the subsequent heating and cooling cycles between 200 and 500 °C. The goal is to simulate the performance of a thermocline tank where the hot and cold molten salts are placed in the same tank. For that reason, the process of charging and discharging the heat is of importance to perform the evolution of the thermocline zone where the heated and cold salts get together. As the test is carried out with two heating mats (HHM and LHM, for the High and Low Heating Mat, respectively) and they have two control systems, they can be operated at different temperatures. Therefore, the charging and discharging process can be performed as described in [18]. The initial state is the end of the drying and dehydration curve when the heat source is at 300 °C. The charging process starts from the top and the heated molten salts come into the tank from the upper part and the cold ones go out of the tank from the bottom. Therefore, the HHM was heated up to 500 °C while the LHM remained constant. After that, the LHM was heated up to 500 °C to simulate a thermocline fully charged. It remained at the maximum temperature for 4 h and then the discharging process was simulated. The discharge is produced backwards, and the heated molten salts go out of the tank from the top and the cold salts come into the tank from the bottom. Given this process, firstly the LHM was cooled down to 200 °C and then the HHM was cooled down to the minimum temperature. Once both heating sources are at 200 °C the thermal cycle is repeated to simulate the thermal fatigue stage.

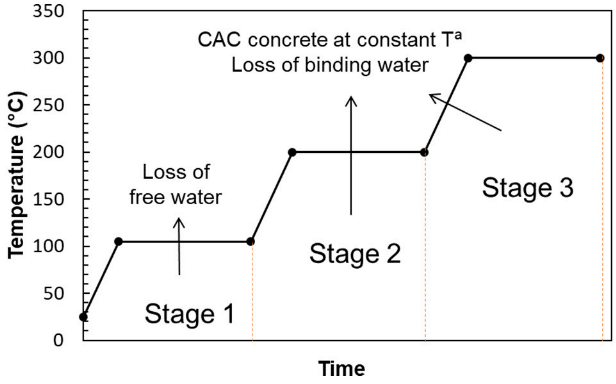

Fig. 4. Drying and dehydration curve.

Fig. 5 shows the thermal cycle followed for the thermal fatigue stage. The plateaus of temperature were maintained for 4 h so as to achieve 1 daily cycle. The first heating up to the maximum temperature (500 °C) was made in order to achieve 300 °C in the air gap. Regarding the cooling process, it followed a natural cooling process. The availability of the workshop for doing the fatigue test was 5 days, so the number of repetitive cycles was 3.

The output parameters measured during the test were the temperature across the concrete at different depths to the heat source and at 3 heights (250, 500 and 750 mm) with conventional thermocouples and temperature and strain at different depths inside the concrete specimen.

2.2.4. Evolution of electrical resistance at high temperature

Additionally, the evolution of the electrical resistance along concrete depth with respect to the heat source was measured. With such aim, the electrical resistance was measured in metallic sheaths located at the depths of 80, 160 and 240 mm. The connections were made by using a wire able to withstand high temperatures, which were connected to the metallic sheaths by using a metallic connector to ensure a suitable assembly. A total of 5 connections were made between the mentioned depths with respect to the heat source as can be appreciated in the view from the top of the concrete layer (Fig. 6). Connection C1 was made between Array E and Array F; C2 between S1 and Array D; C3 between S5 and Array G; C4 between Array A and Array F and C5 between S4 and Array C. Connections C1, C2 and C3 record the evolution of the electrical resistance and, hence, the drying process between 80 and 160 mm of depth with respect to the heat source. On the other hand, connections C4 and C5 register the same parameter between 160 and 240 mm of depth with respect to the heat source.

For measuring the electrical resistance parameter, a data acquisition unit was used. The model was Agilent 34970 A and the data were recorded continuously by using the module Keysight 34901 A. The equipment gives the electrical parameter because it can be recorded by opening one channel of the module directly. The range of measure varies between 0 and 10^8 Ω.

2.2.5. Characterization of concrete layer after the thermal regime

Some analyses were made to the concrete element after the thermal regime in order to evaluate its appropriateness as a CTES at high temperatures. Firstly, a visual analysis of the surface of the concrete was carried out. Secondly, some concrete cores were extracted using a conventional concrete core drill, to have a better knowledge of the heat effect in the core of the concrete. The location of the samples was chosen according to the position of the thermocouples and sensors and were drilled at three different levels: 250, 500 and 750 mm from the top and equidistant. A total of 9 core samples of Φ85x300 mm were extracted. Additionally, samples 2, 5 and 8 were cut into 10 disks of 20 mm, as it is shown in Fig. 7.

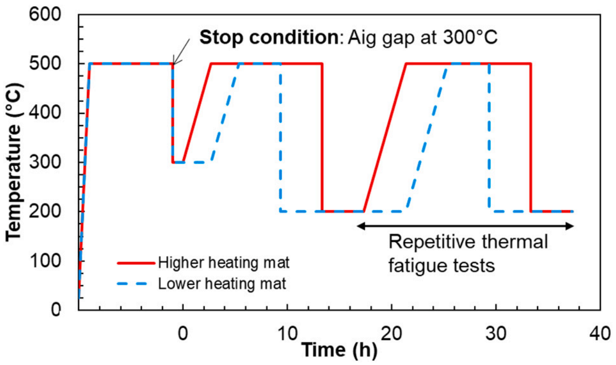

Fig. 5. Thermal fatigue curve.

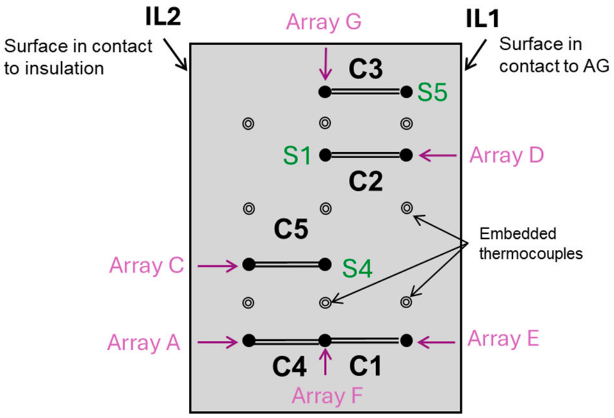

Fig. 6. Schematic representation of the electrical connections at the top of the concrete layer.

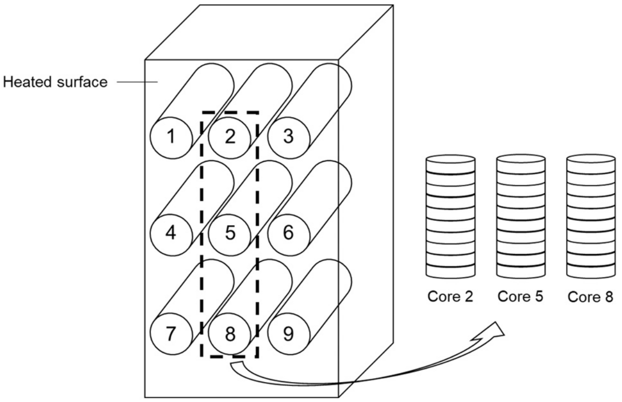

Fig. 7. Position of the drilled core samples of the concrete layer.

The tests that were performed are grouped in two categories: visual analysis and physicochemical characterization and are summarised in Table 4 and Table 5. Firstly, the evolution of the colour profile, the location of sensors and a micro-cracking evaluation was done. For that purpose, the optical microscope SZ61TR from OLYMPUS with a resolution of ±1 μm was used for taking the pictures. Regarding the microcracking analysis, the software OLYMPUS Stream Essentials was employed to quantify the microcracks width. The tests executed for the physicochemical characterization were: compressive strength, evolution of thermal conductivity and electrical resistivity along with the depth, Ultrasonic Pulse Velocity (UPV), accessible water porosity, X-Ray diffraction (DRX) and thermogravimetric analysis (ATD).

Five powder samples were obtained to analyse the DRX and ATD at different depths from the heated surface as follows: 10, 60, 150, 200 and 290 mm. The aim was to detect the chemical transformations in the cement paste across the concrete and the samples were obtained from core 3.

The devices employed for measuring the parameters are as follows: the thermal conductivity equipment was the model QTM-700 from Kyoto Electronics Manufacturing, with an accuracy of ±0.001 W/(m·K). The UPV was obtained by using a PUNDIT 7 CNSFARNELL with a nominal frequency of 54 kHz and a precision of ±0.1 μs. The measurements were made by using two p-wave transducers located in contact with the two parallel surfaces of the concrete disks. The electrical resistivity was obtained from AUTOLAB PGSTAT 302 N Metrohm and it was measured with two metallic grids located in the parallel surfaces of the concrete disks. X-ray diffraction tests (DRX) were carried out on powdered concrete with the equipment BRUKER AXS D8 Advance diffractometer with a RX Lynxeye super speed detector with Cu-Kα radiation and a nickel filter. The samples were scanned from 5 to 45° at 2θ angles with a step size of 0.02° and a counting time of 0.5 s/step. ATD was determined in a TA Instrument, model TGA-DSC-DTA Q600. Finally, the accessible porosity for water in concrete was measured in core samples 2, 5 and 8. The accessible porosity gives the relation between the volume of pores accessible for water and the apparent volume of the sample. The protocol for calculating the porosity followed was UNE 83980. A precision hydrostatic balance was needed for performing the test, model CENT-2 from Gibertini Europe and accuracy of ±0.1 g.

Table 4
Tests of visual analysis of core samples.

Core samples	Visual analyses		
	Colour profile	Location of sensors	Micro-cracking
Left: 1, 4, 7	X	X-	–
Middle: 2, 5, 8	X	X	X
Right: 3, 6, 9	X	X	–

Finally, Table 6 summarises all the stages analysed as well as the tests carried out in the concrete element.

3. Results and discussion

3.1. Setting period

3.1.1. Thermal monitoring

Fig. 8 and Fig. 9 show the evolution of temperature inside concrete recorded by thermocouples and FBG sensors, respectively during cement hydration and the hardening process. Hardening is the process that takes place when concrete is converted into a solid material. Regarding the hydration of the CAC, it records a peak at 10 h between 90 and 110 °C, depending on the location of the sensor (see Fig. 8). The highest temperature was reached in the geometric centre of the specimen (thermocouple 5 and FBG array D).

Regarding the temperature FBGs response, they provided a similar response to the conventional thermocouples. Fig. 9 shows the response of the embedded temperature FBGs placed closest to the conventional thermocouples displayed in Fig. 8, and represented with the same colour code. Array A and Array E, at the Z coordinate of 250 mm (coded A1 and E1) are compared with thermocouples 207 and 209, respectively. Array C at the Z coordinate of 500 mm (C2) is compared with thermocouple 205. Array D and Array G at the Z coordinate of 750 mm (D3 and G3), placed at the bottom of the tank, are compared with thermocouples 203 and 202, respectively. It was observed that the temperature at the centre of the mid-scale tank (500 mm in height) was the highest, followed closely by the temperature at bottom positions (750 mm). The temperature values obtained using the FBGs were in good agreement with the data obtained using the thermocouples (Fig. 10).

The values obtained are consistent with studies that show the peak during the hydration of CAC cement paste around 9 h after the casting [39]. Internal temperatures over 100 °C have also been reported in specific cases, such as curing at 60 °C, where this temperature is reached 3 h after casting [40]. It is important to note that after pouring concrete in the mould, the whole system was completely isolated with Rockwool to avoid the influence of winter weather conditions. For that reason, the heat of hydration was not evacuated quickly. In a real structure of concrete, the peak of hydration depends on the volume and geometry, but it will be lower because the structures are not isolated. However, this experience was useful in determining the construction phases of a real tank structure made of concrete, and the high exothermic reaction of this concrete during the hydration process, was considered for the optimisation of the thermocline tank demonstrator [41].

3.1.2. Strain monitoring

Fig. 11 shows the strain response of the Ni coated embedded FBGs during the first four days of the cement hydration hardening processes in

Table 5
Tests of physicochemical characterization of core samples.

Core samples	Physicochemical characterization						
	Compressive strength	Thermal conductivity	UPV	Electrical resistivity	Porosity	DRX	ATD
Left: 1, 4, 7	–	–	–	–	–	–	–
Middle: 2, 5, 8	–	X	X	X	X	–	–
Right: 3, 6, 9	X	X	X	X	–	Core 3	Core 3

Table 6
Summary of tests performed per stage and the maximum temperature reached within the concrete specimen.

Stages	Setting period	Drying and dehydration	Thermal fatigue cycles	Post-mortem. Residual conditions
Tests	- Thermal monitoring: temperature - Strain monitoring	- Thermal monitoring: temperature - Electrical resistance	- Thermal monitoring: temperature - Strain monitoring - Electrical resistance	-Visual analyses -Physicochemical analyses
Maximum temperature reached in the CAC concrete	110 °C	320 °C	350 °C (when there was 500 °C in the heat source)	Room temperature

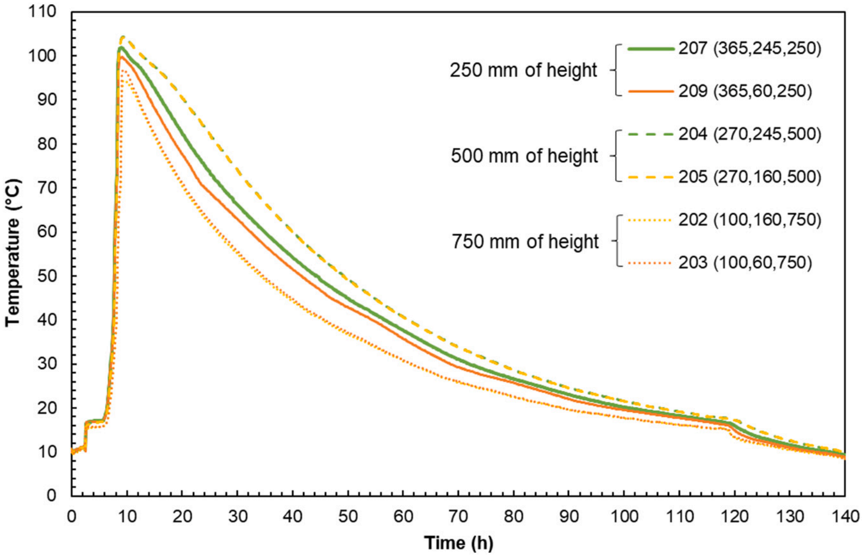

Fig. 8. Evolution of temperature within concrete during the hydration and hardening. Conventional thermocouples.

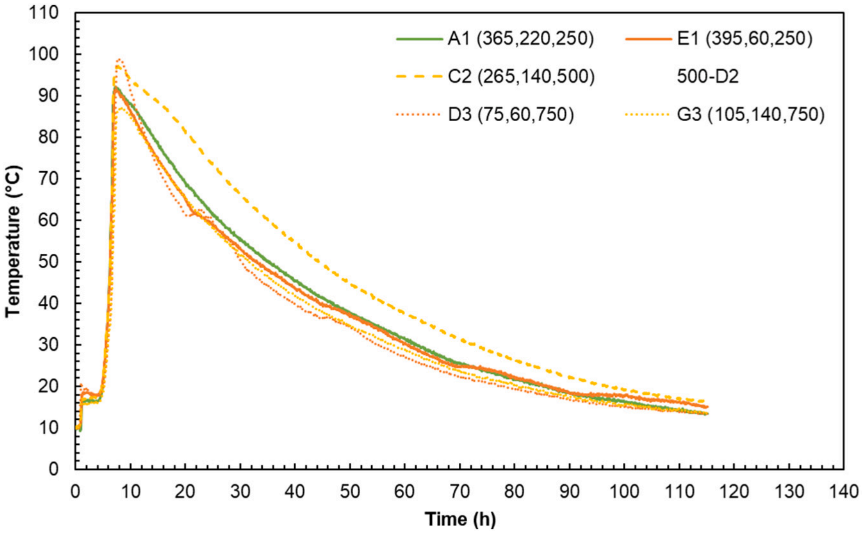

Fig. 9. Temperature FBG sensors response during the hydration and the first hours of hardening process for the FBGs located at the indicated coordinates.

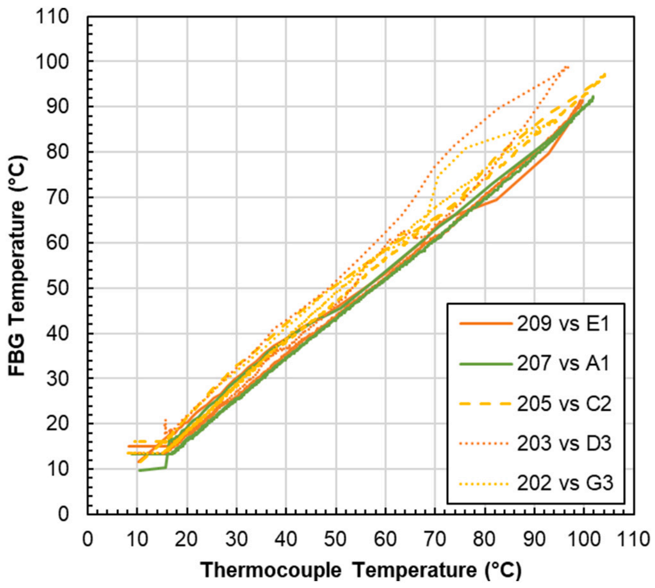

Fig. 10. Comparison of temperatures measured at the FBG sensors and at the conventional thermocouple during the hydration and the first hours of hardening process.

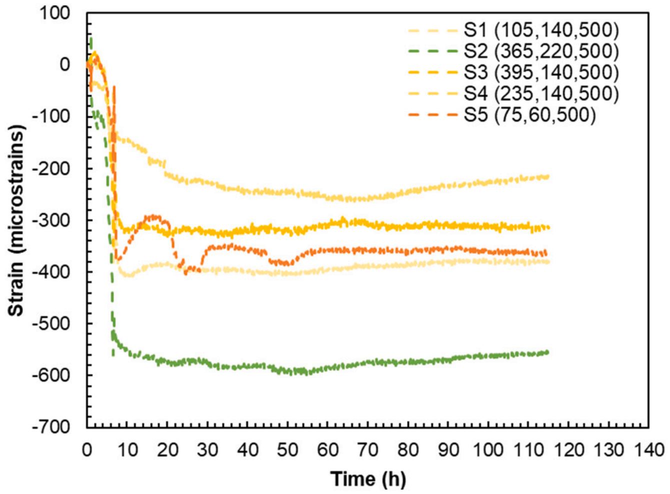

Fig. 11. Strain FBG sensors response during the first four days of curing concrete process.

terms of strain values, (after temperature decoupling). The S2 strain sensor was the sensor which suffers a higher contraction (in the direction of the sensor, i.e. vertically), because it was close to one surface of the thermocline tank layer (Y coordinate 220), and in contrast, the S4 strain sensor suffers a smaller contraction at the end of the hardening process, because it was located in the middle of the concrete layer. Other studies [42] show that CAC based mortars have autogenous and drying shrinkage around 0.02 % and 0.04 % respectively for a similar timeframe, which is equal to 200 and 400 microstrains.

3.2. Drying and dehydration stage

3.2.1. Evolution of temperature across the concrete layer

Fig. 12 shows the evolution of temperature for the 150 h of drying and dehydration stage across the concrete layer. The temperatures are represented in: black for the heat source; red for the boundary surface of the concrete exposed to the air gap; orange, yellow and green for positions inside the concrete layer at different depths and heights (85, 185 and 270 mm, respectively); light blue is the boundary after the CAC layer. Additionally, the temperature recorded at 250, 500 and 750 mm from the top are displayed with a continuous line, a stripped line and a dotted line, respectively. To have a more representative view on the temperature evolution across the concrete layer, the temperature gradients have been represented between layers across the concrete for the three heating steps: 25–100, 100–300, 300–450 °C (Fig. 13). Analysing the monitored temperatures in real time, the heat steps were slightly modified in order to reach a higher temperature in the concrete layer, increasing the time needed for stabilising the temperature to close to 24 h in the 3 plateaus.

The maximum temperature achieved in the concrete layer was around 300 °C and the temperature gradients within the material (ΔT_{CAC}) was 150 °C. At the top, the highest difference in temperatures was achieved in the first 6 cm of CAC concrete layer. Owing to the convection effect in the air gap, this zone was exposed to higher temperatures and underwent the highest heat effect. At the middle and at the bottom, when the temperature increased up to 300–450 °C the highest thermal gradients were obtained between 85 and 185 mm of depth. At the time to stop the test (75 h), the concrete was still raising its temperature and the heat had not arrived at 185 mm. This means that the concrete layer would have needed more time to homogenize the temperature inside and, for that reason, the highest thermal gradients were obtained at those depths. Another influence for this result is that those thermal gradients are measured in longer distances (10 cm in comparison with the first 6 cm).

The evolution of the temperature across the prototype from the heat source to the end of the concrete is shown in Fig. 14 at the end of the drying and dehydration stage, in accordance to the prior paper [18]. The temperature experienced the biggest drop across the CAC concrete layer. Comparing different heights, the top and middle parts followed a similar response in the concrete, but the convection effect is more important at the top.

3.2.2. Electrical resistance during the drying and dehydration

The evolution of the electrical resistance recorded in the 5 connections is displayed in Fig. 15.a. Firstly, the electrical resistance parameter decreases up to 30 h of starting the test, this is considered to be caused by ionic changes produced by the increase of temperature. From that moment, the electrical resistance increases indicating that the concrete layer was losing water from the pores. The rise in the electrical parameter was more significant in regions closer to the heat source as can be seen in the electrical response of connections C1, C2 and C3. At deeper regions, between 160 and 240 mm, the electrical resistance started increasing its value at 60 h and the increase was slower. That is the reason why the curves of connections C4 and C5 experienced a smaller slope.

Regarding the monitoring at different depths, Figure 15Figure 15.b shows the evolution of electrical resistance, as well as the temperature inside the concrete layer at the two levels of depths, evaluated: 80–160 and 160–240 mm. Regarding the region closer to the heat source (80–160 mm), the concrete reached 100 °C after 30 h of starting the thermal exposure, reaching electrical resistance values between 1 and 3 kΩ. By contrast, at depths between 160 and 240 mm the temperature registered 100 °C after 60 h, reaching electrical resistance values of 2–4 kΩ. From that moment, the electrical resistance started growing due to the loss of water and, hence, the drying process. After 75 h, the electrical resistance was among 238–455 kΩ at depths 80–160 mm, whereas the further region (160–240 mm) was reaching values below 30 kΩ. In this way, the level of drying of the concrete layer was lower in that region.

To conclude, the protocol for measuring the drying process of concrete by following the electrical resistance at high temperature has been validated for monitoring the evolution of the loss of water of concrete exposed to heat. Additionally, the protocol allows the monitoring of the drying process at different depths of a concrete infrastructure at large dimensions such as this mock-up section of a thermocline concrete tank

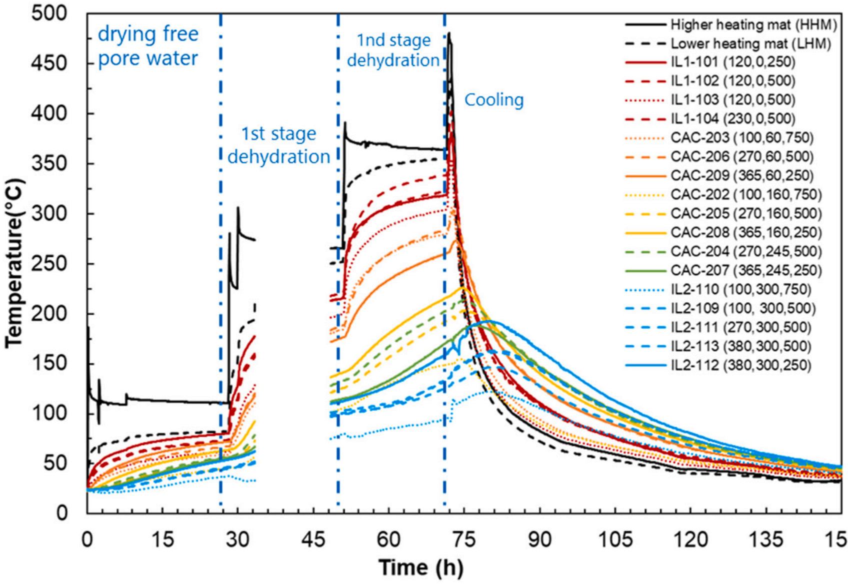

Fig. 12. Evolution of temperature in the layers of the prototype. Drying and dehydration stage.

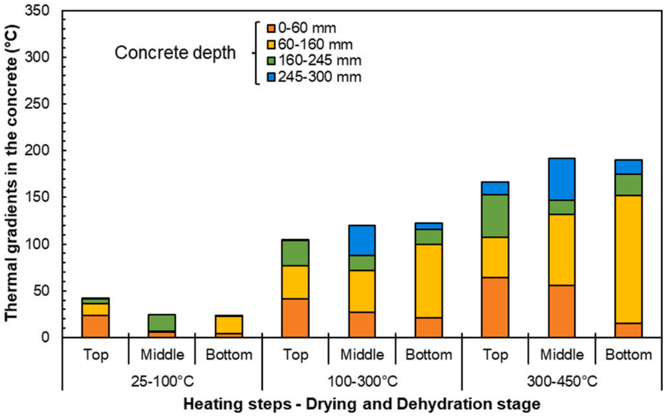

Fig. 13. Thermal gradients in the concrete. Drying and dehydration stage.

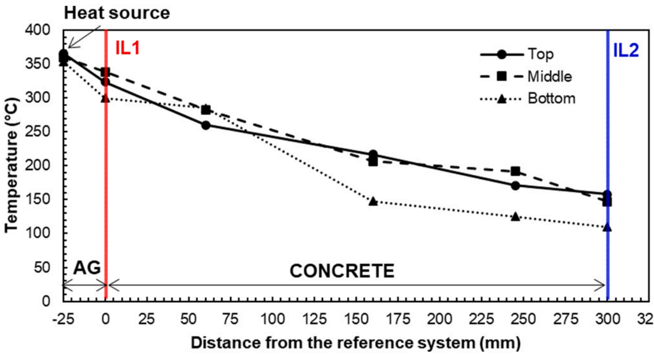

Fig. 14. Evolution of temperature along with the heat source at the end of the drying and dehydration stage, from heat source, surface IL1 and surface IL2.

according to recommendation in [25].

3.3. Thermal fatigue cycles

3.3.1. Evolution of temperature across the concrete layer

The thermal fatigue test consisted of three repetitive heating and cooling cycles. As the test started in another working week, the test starts from room temperature. That is the reason why the first heating was made in order to achieve a temperature of 300 °C in the air gap to simulate the operating condition after the drying and dehydration stage. Once the air gap reached the target temperature, the first cycle started and the heating process up to 500 °C was made according to the procedure described in [18]. Fig. 16 shows the evolution of temperature for the duration of the test across the concrete layer. The temperatures at different depths follow the same colour pattern than in Fig. 12. The thermal gradients across the concrete are represented in Fig. 17 for three scenarios as follows: the first heating up to reach 300 °C in the air gap (initial condition for starting the cycling, time = 3 h), and the maximum and minimum operating temperatures when the heat source was at 500 °C (time = 40 h) and 200 °C (time = 50 h), respectively.

The maximum temperature achieved in the concrete was 350 °C and the temperature gradients within the material (ΔT_{CAC}) was 250 °C. It is worth noting that the closest CAC region (60 mm) to the air gap experienced the highest difference of temperature of 150 °C, due to the reasons explained in the previous section.

The evolution of the temperature from the heat source and across the concrete layer when the heat source was at 500 °C and at 200 °C is shown in Fig. 18. The temperature experienced the biggest drop across the concrete layer when the prototype was operating at the maximum temperature. Comparing different heights, the top and middle part followed a similar response in the concrete, but the convection effect is more important at the top, as it was explained before. When the heat source was at 200 °C, regions closer to the heat source lost energy more quickly, reducing the temperature faster than the regions of concrete located at a deeper distance due to the thermal inertia. The concrete lost energy to the surroundings for the top. For that reason, regions closer to the top reduced their temperature faster than the further ones and this explains why the top and middle remained almost constant along with the distance of the concrete layer.

Regarding FBGs response, Fig. 19 represents a comparison for the temperature FBGs during the thermal tests, showing the comparison of the FBGs located at the same height and the comparison between the FBGs located at a similar location (X, Y) of the mid-scale tank.

Fig. 19 also shows that the temporal response of the temperature FBGs sensors at the higher position reach a higher temperature than the others, as expected, because of the thermal transfer. It is also because the thermal blanket located in the upper half of the mid-scale tank was heating continuously, while the one located in the lower half, was

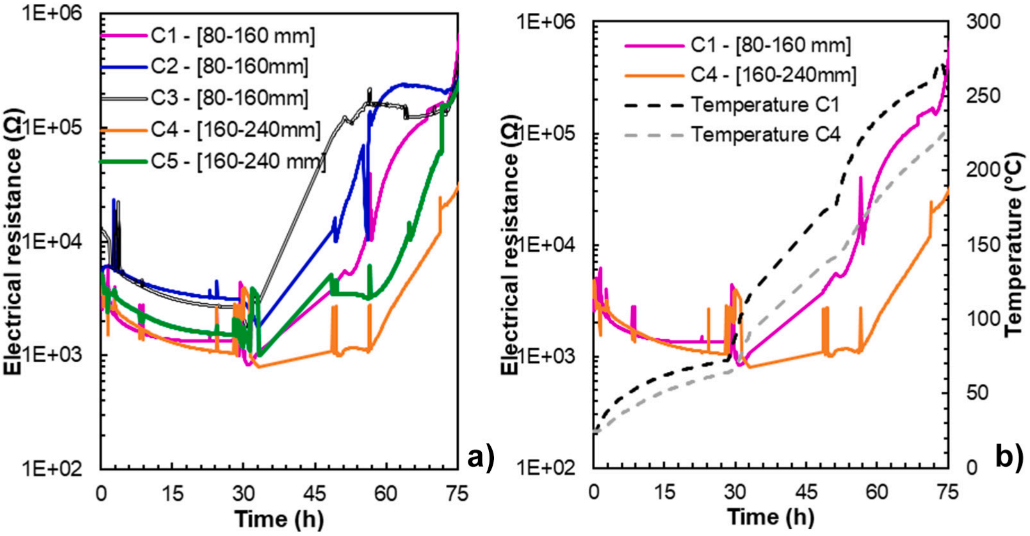

Fig. 15. a) Evolution of the electrical resistance of the 5 connections during the drying and dehydration stage and b) Evolution of electrical resistance and temperature inside the concrete for the 2 levels of depth.

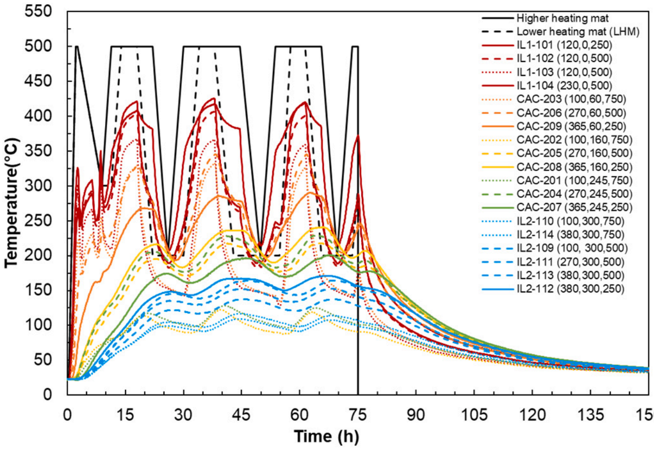

Fig. 16. Evolution of temperature in the layers of the thermocline concrete tank. Thermal fatigue stage.

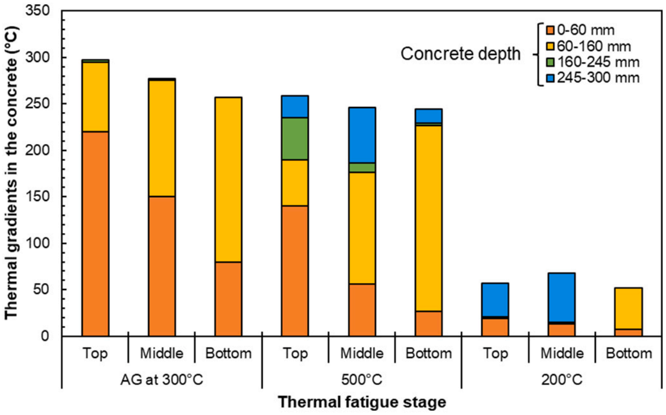

Fig. 17. Thermal gradients in the concrete. Thermal fatigue stage.

turned on and off to simulate the discharge and charge operation. The temperature gradient for the three FBGs of the same array was observed to be between 30 and 50 °C, depending on the sensor location relative to the heat source.

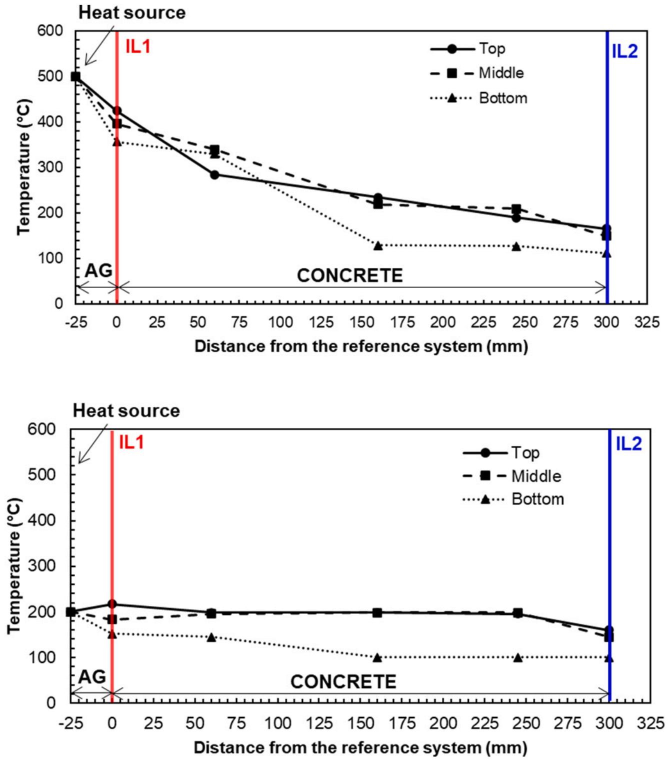

Fig. 18. Evolution of temperature along with the heat source operating at 500 °C (top) and 200 °C (bottom) during the cycling.

In addition, it was also observed that despite the fact that 500 °C was applied on the steel plate, due to the gap, a maximum of only 300 °C was detected in the most proximal zone of the concrete tank section.

Looking at the temperature distribution on the X axis, along a section of the mid-scale tank, FBGs B, D and G are located in the left section of the mid-scale tank, C is located in the central part of the mid-scale tank, and A and F are located in the right section of the mid-scale tank. For the FBGs located in the right part of the concrete tank (seeing the tank from the cold side), it is noticeable that the F sensors reached higher temperatures, but also faster than the A ones due to their proximity to the heating source. The temperature reached has similar to that from arrays

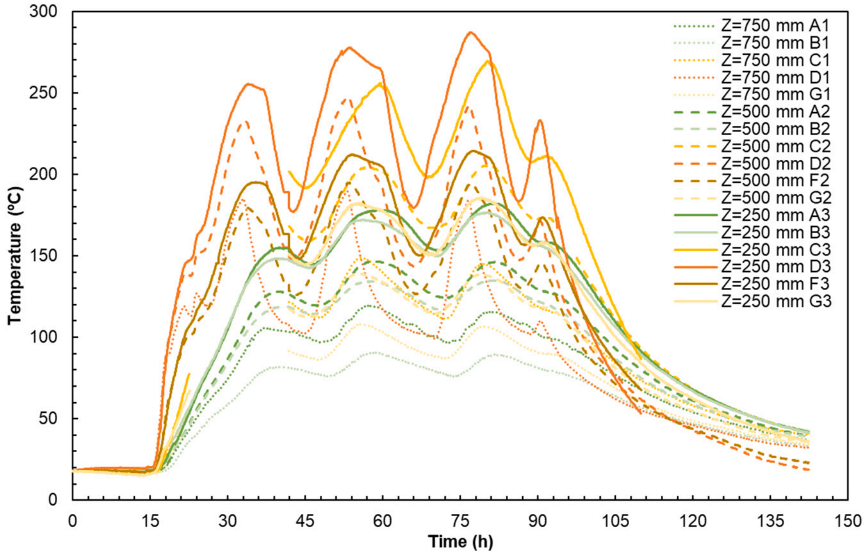

Fig. 19. Detail of the temperature measured by the temperature FBGs at different heights.

G and B located in the left part of the tank section, although array D recorded a higher temperature because it was located closer to the heating source. The temperatures registered in the central part of the tank, by array C, are relative higher than those from left and right parts of the tank but at the same relative position. This means that the concrete concentrates the temperature in the central part.

Using the temperature data recorded with the FBG sensors at different locations and heights of the mid-scale tank section, some interpolations of the data were calculated, obtaining images of the temperature distribution in all the concrete specimen. Fig. 20 represents the interpolated temperature in two different layers of the concrete layer at a specific time of the thermal cycle. The black points of the images represent the location of the FBG sensors embedded into the concrete layer. Fig. 20.a was obtained using the data of sensors in positions B, G, and D, meanwhile, Fig. 20.b was generated with the temperature data from sensors G, C and F.

3.3.2. Strain monitoring

Finally, Fig. 21 shows the comparison between the temperature FBGs C2, and the strain S4 FBG during the thermal test. S4 sensor shows a

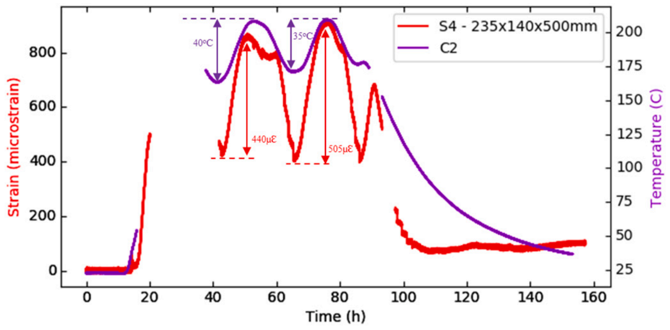

Fig. 21. Comparison for the strain FBGs S4 and temperature C2 FBGs.

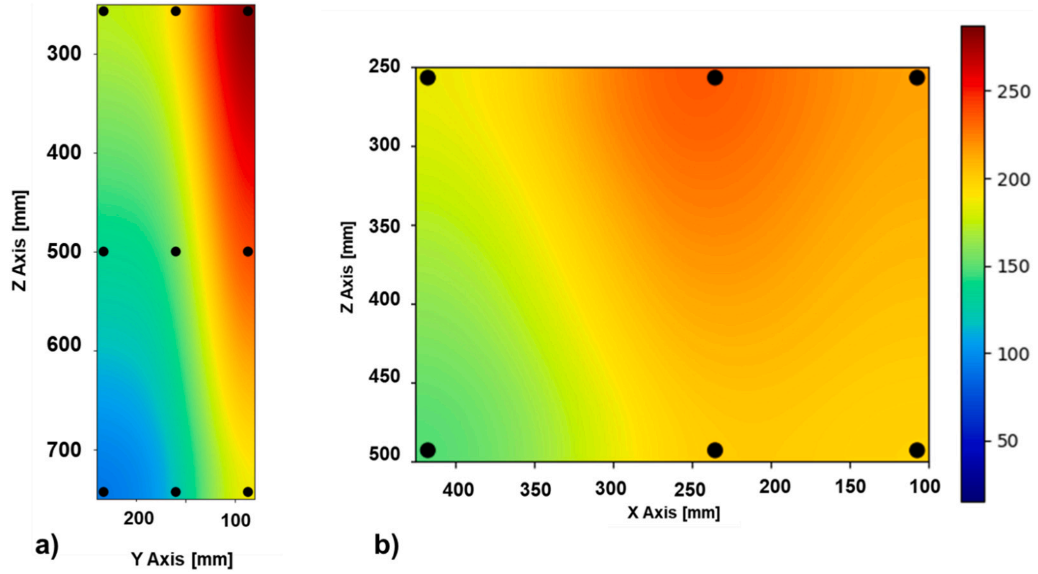

Fig. 20. Representation of the temperature distribution in the concrete layers through the interpolation of the measured data. a) Representation of the temperature gradient for the left side, sensors D, G and B. b) representation of the gradient temperature along the central part of the concrete, sensors G, C and F.

positive strain variation, which means that the FBG detected an expansion, due to the concrete dilatation. The increment measured between the peaks and valleys are 35–40 °C and 440–505 microstrains. Considering an average value for the coefficient of thermal expansion of concrete (α) of 10×10^{-6}/°C, and the equation for thermal strain, $\varepsilon = \alpha \times \Delta T$, a temperature increment of 40 °C would imply a deformation of 400 microstrains, which is within the range of strain measured by the sensors, validating the measures obtained.

3.3.3. Electrical resistance in the thermal fatigue stage

Fig. 22 shows the evolution of the electrical resistance recorded in connection 1 (C1) as well as the temperature measured with thermocouples in regions between 80 and 160 mm from the heat source. Again, the electrical parameter experienced a decrease in its value when the concrete was being heated during the repetitive thermal fatigue cycles. In contrast, the electrical resistance increased during the cooling stages. Nevertheless, the physical explanation of the phenomenon is different to the one presented in the drying and dehydration stage. Once the concrete has been dried and has lost the free water of the pores, concrete conduces the electrical current throughout the cement paste and the solid aggregates. The increase in concrete resistivity with concrete drying has been monitored at temperatures below 100 °C. However, to the authors knowledge, electrical resistance measurements of concrete at these high temperature level have not been found in the literature.

On the other hand, Fig. 23 represents the electrical resistance vs temperature of the concrete for all the heating and cooling phases which took place in the thermal fatigue stage. It is worth noting a non-perfect hysteresis cycle when repeating the thermal cycles. The loops are not overlapped when concrete is at the same temperature and it is explained by the degradation of the concrete when thermal cycling. As the electrical transmission is mainly produced across the solid phases of concrete, the increase in the cement paste microcracking and the gap at the dehydrated cement paste and aggregate interface could be affecting the electrical conduction within the concrete.

3.4. Characterization of concrete after the thermal operation

3.4.1. Visual analysis

The material did not show visual cracks on the surfaces after being exposed to heat and no visual damage was detected. Therefore, the appropriateness of the CAC concrete designed for the thermocline tank wall is once again demonstrated.

3.4.1.1. Deviations of the location of sensors and thermocouples. The location of sensors and thermocouples were identified in the 9 core samples obtained in the concrete. Some of them were identified on the right position and others were missing, indicating that those sensors were moved during casting, concrete pouring and vibration. The position was measured with a calliper and the coordinates for the core sample 1 are shown in Table 7. Sensor input is referred to the top of the core section and sensor output to the bottom part of the section.

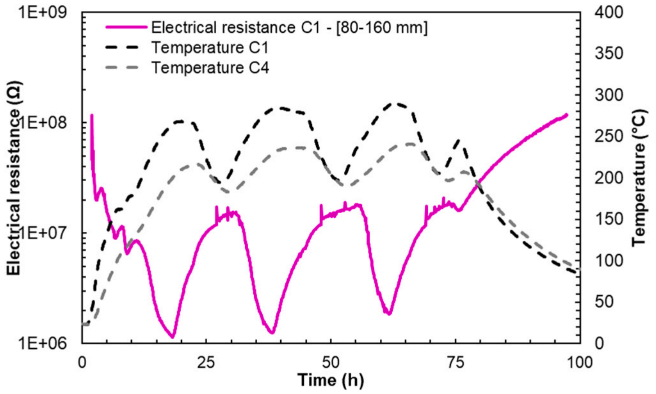

Fig. 22. Evolution of the electrical resistance of connection C1 during the thermal fatigue stage.

3.4.1.2. Colour changes of concrete after heating. The colour profiles were obtained on the surface of the nine drilled core samples. Around 20 pictures were taken by using an optical microscope in order to obtain the profile and to determine the change in the colour. The depth of colour change is related to the maximum temperature achieved in the concrete and, hence, to the chemical transformations of the cement paste due to dehydration. Fig. 24 shows an example of the profile in the core sample 2 from the heated surface (left) to the cooler part (right). The profile represents the first 62.23 mm where the change in colour can be appreciated. The depth of colour change is shown in Fig. 25. Concrete located in the upper part (level 250 mm from the top) underwent a higher depth of colour change. The heat came across higher depth of concrete, around 60 mm whereas the samples located in the lower part (level 750 mm from the top) experienced a colour change within the first 12 mm.

3.4.1.3. Micro-cracking. This analysis was made on the micro-cracks generated along with the depth of the concrete layer. The images were taken for all of the concrete disks from core samples 2 (Fig. 26.a), 5 and 8 in-depth and the crack width was measured in all of them. Fig. 26.b summarises the mean value of the crack widths. On samples located at the top of concrete layer (core 2), the width slightly increases when the distance ranges from 75 to 125 mm, but the cracks are around 30–45 μm. According to the samples located at the middle (core 5), the widths also increase from 50 to 120 mm depth ranging from 10 to 60 μm. On the contrary, sample 8 located at the bottom show scattered values but in any case are the lowest. Those values are in accordance with the micro-crack measurements obtained from different lab-scale studies of CTES [43–45] whose cracks were lower to 80 μm. Nonetheless, the up-scaled concrete structure did not achieve the maximum temperature in deep and the micro-cracks might be created due to the thermal gradients.

3.4.2. Physicochemical characterization

3.4.2.1. Mechanical properties: Compressive strength and Elastic Modulus. The compressive strength and elastic modulus were measured in the core samples located on the right (3, 6 and 9) and the Elastic Modulus was calculated from UPV measurements and are represented in Fig. 27. The core samples also referred as top, middle and bottom were located at 250, 500 and 750 mm from the *Z*-axis in the reference system. Results indicate that the zones located close to the heat source (0–150 mm) were more affected and, hence, the compressive strength was lower than the cooler zones (150–300). Regarding the lower sample (9), the values differ but this could be explained because of the variability of the material. The UPV was measured on core samples located on the middle (2, 5 and 8) and across the depth of the concrete from the heated surface to the coolest region in samples of width around 20 ± 2 mm.

Fig. 28 displays the calculated Elastic Modulus. Results show scatter but two conclusions can be drawn: i) Depths up to 120 mm from the heat source follow the same pattern and the samples located in the upper part had lower velocity, in the same way that samples located on the right (3, 6 and 9), ii) from 125 to 300 mm the velocity in the lower sample (8) is always higher because heat did not arrive and samples 2 and 5 (top and middle, respectively) experienced almost the same values but with higher dispersion.

3.4.2.2. Thermal and electrical properties:. Fig. 29 shows the thermal conductivity (left) and the electrical resistivity (right) measured on drilled core samples 3, 6 and 9. The closest region to the heat source (0 mm) experienced the lowest value of thermal conductivity because of the completely dried and dehydration of the concrete. At higher distance

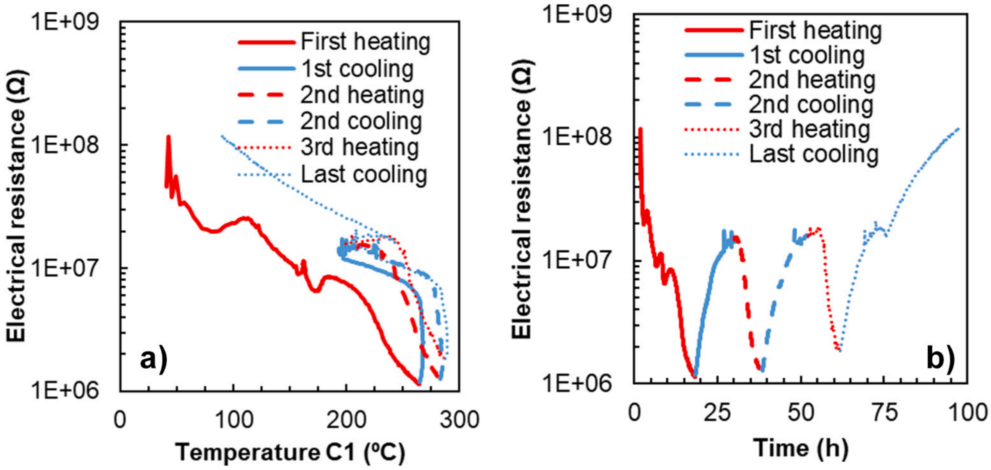

Fig. 23. a) Evolution of electrical resistance with temperature during the thermal fatigue stage and b) electrical resistance with time.

Table 7
Coordinates of sensors located in core sample 1.

	Theoretical position			Measured value					
	Coordinates			Sensor input			Sensor output		
	X	Y	Z	X_1	Y_1	Z_1	X_2	Y_2	Z_2
Core 1	375		250						
	375 ± 42.5		250 ± 42.5						
209	365	60	250	Not located in the core					
208	365	160	250	396	124	213.73	Not located in the core		
207	365	245	250	368.2	210	208.62	Not located in the core		
Array E	395	80	250	406.9	357	224.76	412.9	292.8	268.12
Array F	447	160	250	Not located in the core					
S3	395	160	250	Not located in the core					
Array A	395	240	250	393.65	215	212.1	392.35	210	286.5
S2	365	240	250	364.55	218	210.76	354.91	217	287.82

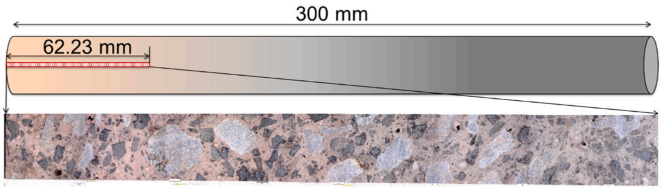

Fig. 24. Colour profile of the core sample 2 in 62.23 mm.

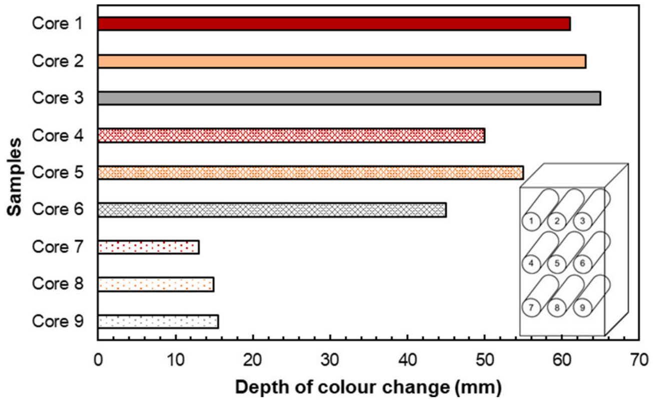

Fig. 25. Depth of colour change of all core samples

to the heated surface, the thermal conductivity was higher because at those locations the temperature was lower and the concrete did not undergo complete dehydration. The value is almost the same at 300 mm in the coolest surface and the high temperature did not arrive at the external surface of the concrete layer. Regarding the electrical resistivity, the samples located near the heat source have higher electrical resistivity than the ones located at 150–300 mm. The reason is that the concrete is more dried and, hence, less electrically conductive. Moreover, the effect of the convection heat transfer mechanism might be detected because the values of electrical resistivity are higher in sample 3 than the core samples 6 and 9. What it does mean is that the upper part of the CAC concrete was more dehydrated because of heat flow.

3.4.2.3. Water accessible porosity of CAC in concrete layer. Fig. 30 shows the changes in the porosity versus depth of concrete. The core 2, located at the top, experienced the highest porosity because the temperature profile through the core 2 achieved a higher temperature and higher dehydration level of cement paste. The core 5, located at the middle, followed the same pattern but with lower porosity. Regarding the core 8, it is remarkable the decrease in the second half of the sample, from 150 to 300 mm, achieving 15.5 % of porosity at the end. This value is typical for the concrete without being exposed to a heat source.

3.4.2.4. Microstructural changes: XDR and TG/DTA. X-ray diffraction (DRX) performed on concrete powder samples (Fig. 31.a) show the presence of several phases associated with the hydrated compounds (C_2AH_6, CAH_{10} and AH_3), which disappear after being exposed to heat at 1 and 6 cm. For deeper samples, the presence of the hydrated compounds indicates that the cement paste was not dehydrated and the

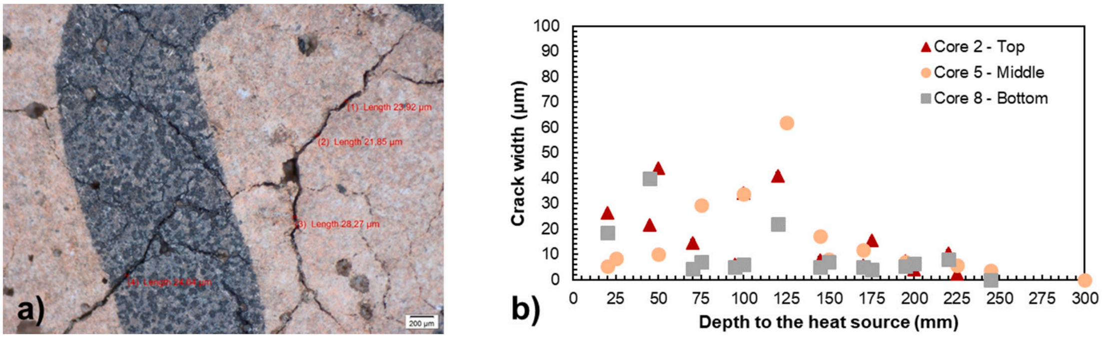

Fig. 26. a) Cracks appearance in one of the cores analysed, b) Crack width with depth from the heat source

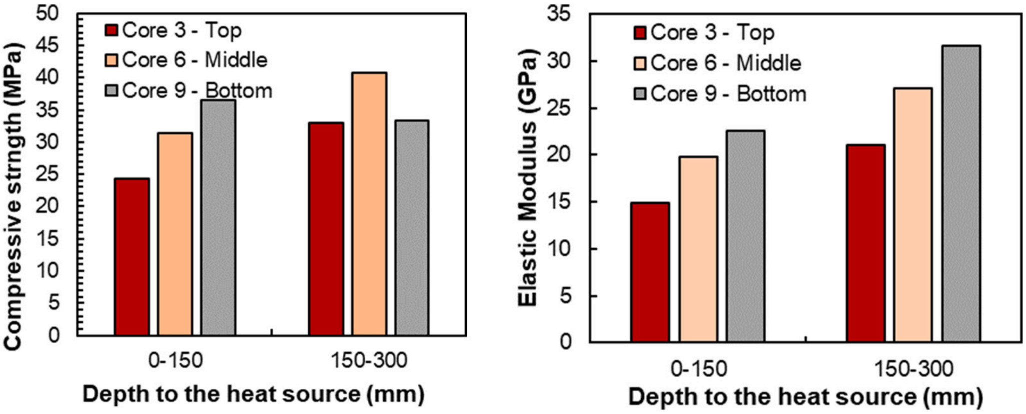

Fig. 27. Compressive strength and Elastic modulus in core samples 3, 6 and 9.

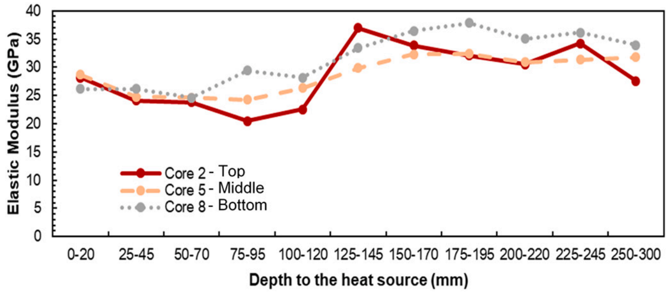

Fig. 28. Elastic modulus in core samples 2, 5 and 8 along with the depth of the concrete to the heat source.

temperatures at those locations were lower to 300 °C. The remaining phases are related with the spectra of unhydrated calcium aluminate (CA and $C_{12}A_7$), produced by both the unhydrated cement and the CAT aggregates, but also quartz originated in the basalt aggregates, which are rich in silicon, and calcite, which can be formed due to the calcium-rich cement paste. Those phases might be appreciated at 6, 15, 20 and 29 cm and indicate that the concrete was not dehydrated at those positions.

The TG/dTG results are displayed in Fig. 31.b at 1, 6, 15, 20 and 29 cm from the heated surface. The peaks in the dTG curve show transformations produced by dehydration of CAH_{10} and C_2AH_8 between 120 and 200 °C and to dehydration of AH_3 between 200 and 240 °C. Other transformations at 450–500 °C and 700 °C might be associated with *Alentejo* Slag Aggregates and calcium carbonate, respectively. The results show clear differences between the samples located at 1 and 6 cm and the other ones. The weight loss was 5.6 % and 6.67 % for samples

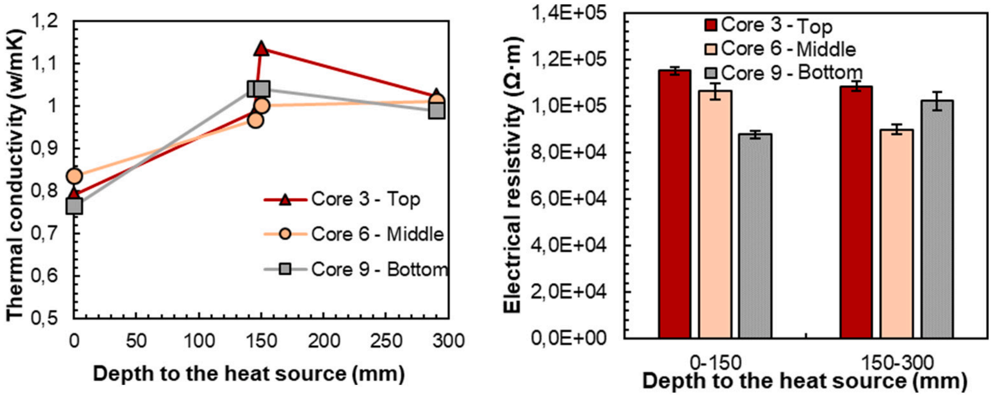

Fig. 29. Thermal conductivity and electrical resistance of samples 3, 6 and 9 measured at residual conditions.

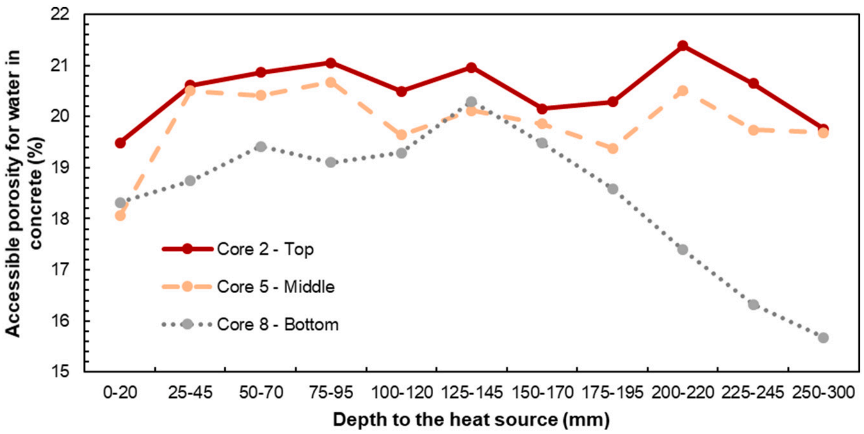

Fig. 30. Evolution in depth of accessible porosity of samples 2, 5 and 8.

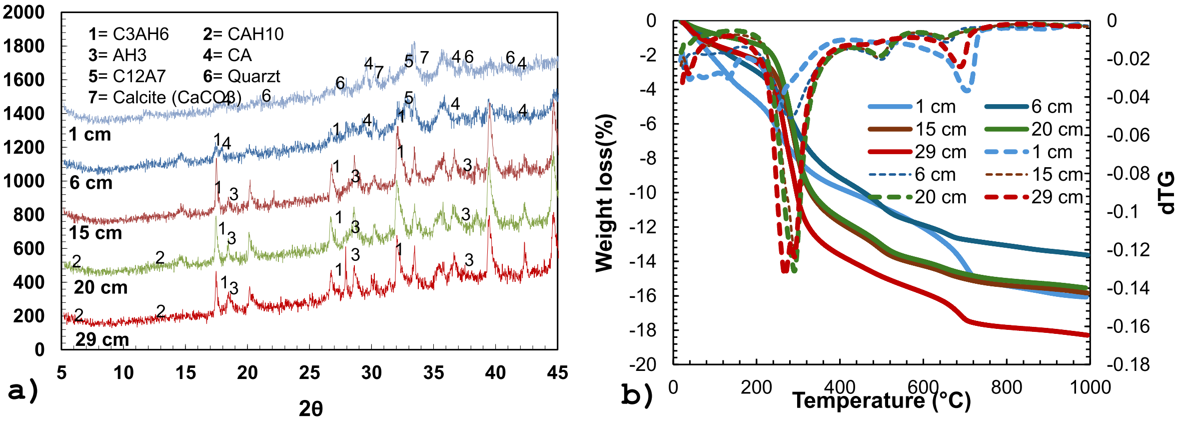

Fig. 31. a) XRD results of CAC concrete samples at 1, 6, 15, 20 and 29 cm from the heated surface, b) The TG/dTG results at 1, 6, 15, 20 and 29 cm from the heated surface.

located at 1 and 6 cm, respectively. Those samples experienced a lower peak of transformation at 270 °C, indicating that most of the CAC were dehydrated in the thermal performance of the concrete layer. On the contrary, samples at 15, 20 and 29 cm experienced a loss of 10.01 %, 10.48 % and 11.96 %, respectively. Samples located at a deeper distance from the heat source underwent higher peak of transformation, which indicates that the cement was not dehydrated at those regions.

4. Conclusions

The experimental analysis of the thermal performance of a prototype of a thermocline tank made of CAC concrete was carried out. The evolution of the CAC concrete layer thermal response subjected to a heat source ranging from 200 to 500 °C was investigated in depth and monitored throughout the different heating stages. Based on the experimental results presented in this work, the following conclusions have been drawn:

- CAC concrete is a feasible material for this high temperature application, the mix composition used showed appropriate compressive strength values. The final CAC concrete layer has been able to withstand gradients of temperature during the cyclic operation, with only minor cracks, and maintaining reasonable thermomechanical properties after the operation.
- Innovative sensors and methodologies have been validated during CAC validation (hardening and thermal cycles). Ad-hoc Fiber Bragg Grating (FBG) sensors were validated to measure both temperature and strain at high temperatures continuously. The temperature obtained from the thermocouples and the temperature FBG sensors is almost equal. In the case of strains, the values obtained are within the expected range of values. Resistivity measurements allowed to identify the drying process and the thermal changes during thermal cycles carried-out.
- During the setting period, concrete has an exothermic reaction during the hydration process and the temperatures measured reached 100 °C. After the first hours, the concrete tank section is contracting slowly, and the temperature variations registered are due to the environmental conditions. Strain sensors placed close to the surface suffered a higher contraction while the sensor placed in the centre of the tank suffered a higher expansion during the hydration phase and a smaller contraction at the end of the hardening process.
- During the drying and dehydration stage, the electrical resistance decreased with temperature up to 100 °C, and then increased while the concrete was being heated. The maximum temperature achieved in the CAC concrete was 300 °C and the temperature gradient within the material was 150 °C.
- During the thermal fatigue stage, the maximum temperature achieved in the CAC concrete was 350 °C and the temperature gradient within the material was 250 °C. The sensor placed in the centre of the element, shows a positive strain variation, indicating an expansion due to the concrete dilatation. The electrical resistance decreased when concrete was being heated and increased during the cooling stages, and a non-perfect hysteresis cycle was registered when repeating the thermal cycles, which indicates indirectly the degradation (such as cracks) produced in the material.

- The characterization of CAC concrete in drilled core samples obtained after the complete operation validates this material for this application. The colour change reported is related to the maximum temperature achieved and the chemical transformations of the cement paste, and the cracks generated are below 60 μm generally. The compressive strength measured was over 25 MPa, and the elastic modulus measured by UPV ranges from 15 to 35 GPa. The positions exposed to the highest temperatures, had decreased thermal conductivity, increased electrical resistance and increased porosity, which indicate that parts of the CAC layer did not experience complete dehydration. In addition, XRD showed remaining hydrated phases (C_2AH_6, CAH_{10} and AH_3) in positions with temperatures below 300 °C, and unhydrated phases (CA and $C_{12}A_7$) in positions that underwent complete dehydration. TG/dTG corroborate these results showing that CAH_{10} and C_2AH_8 dehydrate between 120 and 200 °C and AH_3 between 200 and 240 °C.

CRediT authorship contribution statement

T. Lucio-Martin: Writing – original draft, Methodology, Investigation, Conceptualization. **T. Grandal:** Writing – original draft, Validation, Resources, Methodology, Investigation, Conceptualization. **M. Roig-Flores:** Writing – review & editing, Methodology, Investigation, Conceptualization. **R.S. Villardón:** Validation, Methodology, Investigation, Data curation. **Luis Guerreiro:** Writing – review & editing, Project administration, Funding acquisition, Conceptualization. **M.C. Alonso:** Writing – review & editing, Supervision, Methodology, Investigation, Funding acquisition, Conceptualization.

Declaration of competing interest

The authors declare that they have no known competing financial interests or personal relationships that could have appeared to influence the work reported in this paper.

Acknowledgments

The research was financially supported by the H2020 project NewSol, New StOrage Latent and sensible concept for high efficient CSP Plants (Project ID: 720985). The authors would also like to thank *Cement Molins* for providing CAC and CAT and for the technical discussions.

Data availability

Data will be made available on request.

References

[1] M.A. Hannan, A.Q. Al-Shetwi, R.A. Begum, P.J. Ker, S.A. Rahman, M. Mansor, M. S. Mia, K.M. Muttaqi, Z.Y. Dong, Impact assessment of battery energy storage systems towards achieving sustainable development goals, J. Energy Storage 42 (2021) 103040.

[2] A. Gil, M. Medrano, I. Martorell, A. Lázaro, P. Dolado, B. Zalba, L.F. Cabeza, State of the art on high temperature thermal energy storage for power generation. Part 1—concepts, materials and modellization, Renew. Sust. Energ. Rev. 14 (2010) 31–55.

[3] V.D. Cao, S. Pilehvar, C. Salas-Bringas, A.M. Szczotok, J.F. Rodriguez, M. Carmona, N. Al-Manasir, A. Kjøniksen, Microencapsulated phase change materials for enhancing the thermal performance of Portland cement concrete and geopolymer concrete for passive building applications, Energy Convers. Manag. 133 (2017) 56–66.

[4] L.F. Cabeza, L. Navarro, A.L. Pisello, L. Olivieri, C. Bartolomé, J. Sánchez, S. Álvarez, J.A. Tenorio, Behaviour of a concrete wall containing micro-encapsulated PCM after a decade of its construction, Sol. Energy 200 (2020) 108–113.

[5] Y. Liu, M. Xie, E. Xu, X. Gao, Y. Yang, H. Deng, Development of calcium silicate-coated expanded clay based form-stable phase change materials for enhancing thermal and mechanical properties of cement-based composite, Sol. Energy 174 (2018) 24–34.

[6] E. John, M. Hale, P. Selvam, Concrete as a thermal energy storage medium for thermocline solar energy storage systems, Sol. Energy 96 (2013) 194–204.

[7] M.C. Alonso, J. Vera-Agullo, L. Guerreiro, V. Flor-Laguna, M. Sanchez, M. Collares-Pereira, Calcium aluminate based cement for concrete to be used as thermal energy storage in solar thermal electricity plants, Cem. Concr. Res. 82 (2016) 74–86.

[8] V.A. Salomoni, C.E. Majorana, G.M. Giannuzzi, A. Miliozzi, R. Di Maggio, F. Girardi, D. Mele, M. Lucentini, Thermal storage of sensible heat using concrete modules in solar power plants, Sol. Energy 103 (2014) 303–315.

[9] D. Laing, C. Bahl, T. Bauer, M. Fiss, N. Breidenbach, M. Hempel, High-temperature solid-media thermal energy storage for solar thermal power plants, Proc. IEEE 100 (2012) 516–524.

[10] N. Hoivik, C. Greiner, J. Barragan, A.C. Iniesta, G. Skeie, P. Bergan, P. Blanco-Rodriguez, N. Calvet, Long-term performance results of concrete-based modular thermal energy storage system, J. Energy Storage 24 (2019) 100735.

[11] V.A. Sötz, A. Bonk, J. Forstner, T. Bauer, Molten salt chemistry in nitrate salt storage systems: linking experiments and modeling, Energy Procedia 155 (2018) 503–513.

[12] S. Ushak, A.G. Fernández, M. Grageda, 3 - using molten salts and other liquid sensible storage media in thermal energy storage (TES) systems, Adv. Thermal Energy Storage Syst. (2015) 49–63.

[13] A. Bonk, M. Braun, V.A. Sötz, T. Bauer, Solar salt – pushing an old material for energy storage to a new limit, Appl. Energy 262 (2020) 114535.

[14] Z. Ma, P. Davenport, R. Zhang, Design analysis of a particle-based thermal energy storage system for concentrating solar power or grid energy storage, J. Energy Storage 29 (2020) 101382.

[15] E. John, M. Hale, P. Selvam, Concrete as a thermal energy storage medium for thermocline solar energy storage systems, Sol. Energy 96 (2013) 194–204.

[16] J. López Sanz, F. Cabello Nuñez, F. Zaversky, Benchmarking analysis of a novel thermocline hybrid thermal energy storage system using steelmaking slag pebbles as packed-bed filler material for central receiver applications, Sol. Energy 188 (2019) 644–654.

[17] A. Modi, C.D. Pérez-Segarra, Thermocline thermal storage systems for concentrated solar power plants: one-dimensional numerical model and comparative analysis, Sol. Energy 100 (2014) 84–93.

[18] T. Lucio-Martin, M. Martin, L. Guerreiro, R.S. Villardón, J. Lopez, M.C. Alonso, Thermal performance of a hybrid steel-concrete tank section for thermal energy storage in concentrated solar power plants, J. Energy Storage 60 (2023) 106630.

[19] M. Roig-Flores, T. Lucio-Martin, M.C. Alonso, L. Guerreiro, Evolution of thermo-mechanical properties of concrete with calcium aluminate cement and special aggregates for energy storage, Cem.Concr.Res. 141 (2021).

[20] T. Lucio-Martin, M. Roig-Flores, M. Izquierdo, M.C. Alonso, Thermal conductivity of concrete at high temperatures for thermal energy storage applications: experimental analysis, Sol. Energy 214 (2021) 430–442.

[21] Z.P. Bažant, M.F. Kaplan, Z.P. Bazant, Concrete at High Temperatures: Material Properties and Mathematical Models, 1996.

[22] P. Pimienta, R.J. McNamee, J. Mindeguia, Physical Properties and Behaviour of High-Performance Concrete at High Temperature, Springer, 2018.

[23] W. Khaliq, H.A. Khan, High temperature material properties of calcium aluminate cement concrete, Constr.Build.Mater. 94 (2015) 475–487.

[24] T. Lucio Martín, Sensible Heat Storage in Cement-Based Materials for Solar Thermal Power Plants Infrastructures, 2021.

[25] T. Lucio Martin, M. Alonso Alonso, Measuring Method and Measuring Device for Continuous Non-destructive Detection of the Drying of a Concrete Structure, 2020.

[26] I. Hansson, C.M. Hansson, Electrical resistivity measurements of Portland cement based materials, Cem.Concr.Res. 13 (1983) 675–683.

[27] B. Han, S. Ding, X. Yu, “Intrinsic self-sensing concrete and structures: a review,” Measurement, J. Int. Meas. Confed. 59 (2015) 110–128.

[28] Y.B. Lin, J.C. Chern, K. Chang, Y. Chan, L.A. Wang, The utilization of fiber Bragg grating sensors to monitor high performance concrete at elevated temperature, Smart Mater.Struct. 13 (2004) 784.

[29] D.B. Le, S.D. Tran, V.T. Dao, J. Torero, Deformation capturing of concrete structures at elevated temperatures, Procedia Eng. 210 (2017) 613–621.

[30] L.S. Alwis, K. Bremer, B. Roth, Fiber optic sensors embedded in textile-reinforced concrete for smart structural health monitoring: a review, Sensors 21 (2021) 4948.

[31] A. Amaya, J. Sierra-Pérez, Toward a structural health monitoring methodology for concrete structures under dynamic loads using embedded FBG sensors and strain mapping techniques, Sensors 22 (2022) 4569.

[32] K. Kesavan, K. Ravisankar, S. Parivallal, P. Sreeshylam, S. Sridhar, Experimental studies on fiber optic sensors embedded in concrete, Measurement 43 (2010) 157–163.

[33] R.H. Scott, S. Chikermane, M. Vidakovic, B. McKinley, T. Sun, P. Banerji, K. T. Grattan, Development of low cost packaged fibre optic sensors for use in reinforced concrete structures, Measurement 135 (2019) 617–624.

[34] SHM System, "DFOS measurements by Nerve-Sensors,".

[35] R. Pérez-López, A.M. Álvarez-Valero, J.M. Nieto, R. Sáez, J.X. Matos, Use of sequential extraction procedure for assessing the environmental impact at regional scale of the São Domingos mine (Iberian Pyrite Belt), Appl. Geochem. 23 (2008) 3452–3463.

[36] H. Freitas, M.N.V. Prasad, J. Pratas, Plant community tolerant to trace elements growing on the degraded soils of São Domingos mine in the south east of Portugal: environmental implications, Environ. Int. 30 (2004) 65–72.

[37] M. Zeiml, D. Leithner, R. Lackner, H.A. Mang, How do polypropylene fibers improve the spalling behavior of in-situ concrete? Cem. Concr. Res. 36 (2006) 929–942.

[38] D. Laing, C. Bahl, T. Bauer, M. Fiss, N. Breidenbach, M. Hempel, High-temperature solid-media thermal energy storage for solar thermal power plants, Proc. IEEE 100 (2011) 516–524.

[39] M.d.M. Alonso, M. Palacios, F. Puertas, Effect of Polycarboxylate–Ether Admixtures on Calcium Aluminate Cement Pastes. Part 2: Hydration Studies, Ind. Eng. Chem. Res. 52 (2013) 17330–17340.

[40] L. Boquera, J.R. Castro, A.L. Pisello, C. Fabiani, A. D'Alessandro, F. Ubertini, L. F. Cabeza, Effect of the curing process on the thermomechanical properties of calcium aluminate cement paste under thermal cycling at high temperatures for thermal energy storage applications, J. Energy Storage 56 (2022) 106039.

[41] T. González, Metal Coating and Embedding Fibre Optical Sensors for Industrial Applications, 2023.

[42] J.L. García-Calvo, M. Sánchez, L. Fernández-Luco, M.C. Alonso, Shrinkage behaviour and related corrosion performance of low-pH cementitious materials based on OPC or CAC, Mater. Constr. 66 (2016) e079.

[43] T. Lucio-Martin, M. Roig-Flores, M.C. Alonso and L. Guerreiro, "Evolution of thermal conductivity on CAC concrete at high temperatures and during thermal fatigue tests." vol. Proceedings of the 6th International Workshop on Concrete Spalling due to Fire Exposure, 2019.

[44] T. Lucio-Martin, J. Puentes and M.C. Alonso, "Effect of geometry in concrete spalling risk subjected to high temperatures for thermal inertia studies," vol. Proceedings of the 6th International Workshop on Concrete Spalling due to Fire Exposure, pp. 71–80, 2019.

[45] M.C. Alonso, J. Puentes, Self-compacted concrete with self-protection and self-sensing functionality for energy infrastructures, Materials 13 (2020) 1106.